Original contribution

A new RF transmit coil for foot and ankle imaging at 7T MRI

Tales Santini[a], Junghwan Kim[a], Sossena Wood[a], Narayanan Krishnamurthy[a], Nadim Farhat[a], Carlos Maciel[b], Shaileshkumar B. Raval[a], Tiejun Zhao[c], Tamer S. Ibrahim[a,d,*]

[a] University of Pittsburgh, Department of Bioengineering, United States
[b] University of Sao Paulo, Department of Electrical and Computer Engineering, Brazil
[c] Siemens Medical Solutions, United States
[d] University of Pittsburgh, Department of Radiology, United States

ABSTRACT

A four-channel Tic-Tac-Toe (TTT) transmit RF coil was designed and constructed for foot and ankle imaging at 7T MRI. Numerical simulations using an in-house developed FDTD package and experimental analyses using a homogenous phantom show an excellent agreement in terms of B_1^+ field distribution and s-parameters. Simulations performed on an anatomically detailed human lower leg model demonstrated an B_1^+ field distribution with a coefficient of variation (CV) of 23.9%/15.6%/28.8% and average B_1^+ of 0.33 μT/0.56 μT/0.43 μT for 1 W input power (i.e., 0.25 W per channel) in the ankle/calcaneus/mid foot respectively. In-vivo B_1^+ mapping shows an average B_1^+ of 0.29 μT over the entire foot/ankle. This newly developed RF coil also presents acceptable levels of average SAR (0.07 W/kg for 10 g per 1 W of input power) and peak SAR (0.34 W/kg for 10 g per 1 W of input power) over the whole lower leg. Preliminary in-vivo images in the foot/ankle were acquired using the T2-DESS MRI sequence without the use of a dedicated receive-only array.

1. Introduction

Magnetic resonance imaging (MRI) has been used to investigate a wide range of abnormalities, injuries and diseases related to musculoskeletal tissues, such as cartilage degeneration [1,2], bone marrow edemas [3], osteoarthritis [2–5], osteoporosis [2,6], and ligament/tendon insures [5,7]. While most of the clinical applications relies on images acquired at 1.5 or 3 Tesla (T) scanners, the enhanced contrast and signal-to-noise ratio (SNR) provided by ultra-high field (UHF, ≥ 7T) MRI can be highly attractive for musculoskeletal imaging [8]. The increased SNR can be traded to increase the spatial resolution of the images [9] or to decrease the scan time [10] (although the T1 relaxation is longer at UHF, higher levels of accelerations can used due to the increased SNR). On the other hand, the increased B_1^+ (circularly polarized magnetic field responsible for excitation) inhomogeneities, increased chemical shift, and increased peak and average specific absorption ratio (SAR) present great challenges in the translation of the UHF research to a reliable clinical standard [11].

To address the problems in B_1^+ inhomogeneity and high SAR, multi-channel radiofrequency coils have been developed for various parts of the body [12]. Moreover, due to the lack of integrated body coil in UHF scanners (usually available at 1.5T and 3T scanners), the radiofrequency (RF) coil must work as either a transceiver or transmit

(Tx)-only/receive (Rx)-only pairs should be built. Additionally, RF shimming techniques can potentially improve the B_1^+ homogeneity and efficiency in a specific region of interest, while reducing the global and local SAR [13–15].

To the best of our knowledge, there are few research groups that have developed RF coils specific for 7T imaging of the foot/ankle [16,17], as most of the studies use commercial knee coils [7,18–22] or head coils [23–26] for imaging these parts of the body. This is not optimal because the subject may be asked to stay in an uncomfortable position (e.g., foot in a high angle) and the coil may not be suitable and/or optimal for all foot sizes.

In this study, we provide details and design parameters for a 7T transmit (Tx) RF coil dedicated for foot and ankle imaging. The design was adapted from the Tic-Tac-Toe (TTT) concept utilized in imaging for a wide variety of body organs at 7T [27–32]. The coil's magnetic and electric field distributions, input impedance, coupling matrix were simulated using the finite-difference time-domain (FDTD) method in a homogenous cylindrical phantom model. The B_1^+ maps and scattering parameters of the constructed RF coil were experimentally measured in a cylindrical phantom with assigned conductivity and permittivity equal to the average values present in the lower leg of the Duke model (IT'IS Foundation, Switzerland) and the results were compared with the simulations. The coil's SAR and B_1^+ field distributions calculated inside
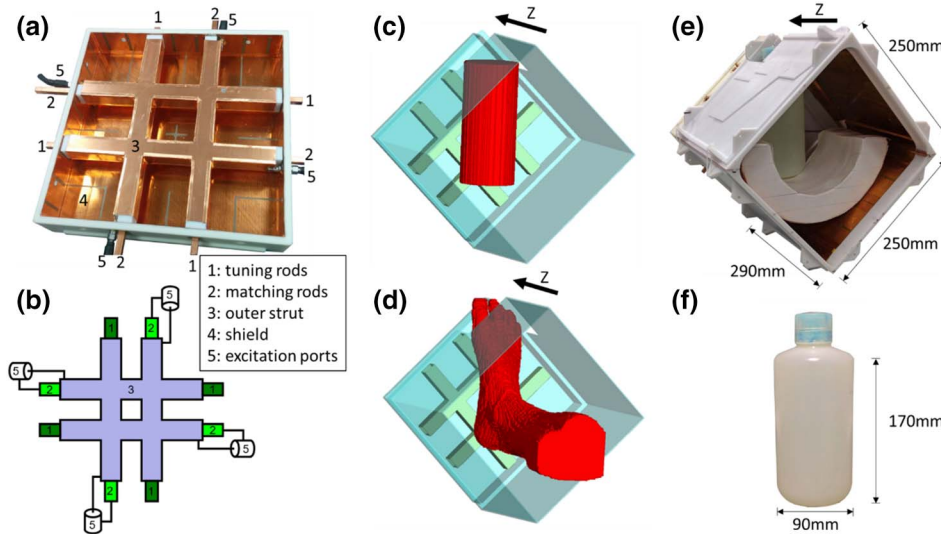
Fig. 1. Design of the TTT foot and ankle Tx RF coil. In (a), the assembled coil without the shielding frame. In (b), the schematic of the RF coil. In (c), the FDTD grid of the simulated coil with a homogenous phantom as the load. In (d), the FDTD grid of the RF coil including the right lower leg model extracted from Duke model. In (e), the assembled coil, with the external shielding frame and the homogenous phantom. In (f), the homogeneous phantom used in the B_1^+ map acquisition, having relative permittivity of 39 and conductivity of 0.49 S/m (average values from the lower leg of the Duke model).

Duke's anatomically detailed lower leg human model were also attained using FDTD method. Finally and only for demonstration purposes, in-vivo B_1^+ mapping and preliminary images using T2-DESS sequence were acquired without the use of a dedicated Rx-only insert.

2. Materials and methods

2.1. Tx RF coil design

A Tx RF coil for foot and ankle imaging at 7T was designed based on the TTT family (a Tx RF coil design inspired by the arrangement of cross-pole antennas [27–31,33,34]). The Tx RF coil is composed of eight squared-shape transmission lines, electrically connected to each other in a 2×2 Tic-Tac-Toe format (Fig. 1a and b). The dimensions of the coil were 228.6×228.6 mm^2 in XY directions and 16.8 mm in Z direction, which is the direction of the static magnetic field (B$_0$) (see Fig. 1a). The inner rods of the transmission lines were made of solid squared-shape copper (McMaster-Carr, USA), with the cross-section dimensions of 6.35×6.35 mm^2 (see Fig. 1b). The outer strut was built from an 8 μm think single-layered copper sheet (Polyflon, Germany). A 3D-printed polycarbonate inner dielectric was designed using Solidworks (Solidworks, USA); it offered support for both the inner rods and outer struts, and defined the relative permittivity of the inner core of the transmission line to be equal to 2.4. The complete assembly of the 4-channel transmit array is shown in the Fig. 1a.

The center pin of the excitation transmission lines was connected to the outer strut of the coil while the inner rod was connected to the shield/ground. Matching and tuning rods were placed in an alternated fashion, so that the coil had 4 excitation ports with matching rods, and 4 tuning rods, without excitation (Fig. 1b). The Tx RF coil can be tuned and matched to 50 Ω at 297.2 MHz (Larmor frequency for ^{1}H at 7T) by changing the rods' lengths, which affect the coil reactance and allows the resonant frequency of the RF circuit to be adjusted to the scanner's Larmor frequency.

2.2. Design of RF shielding

An RF shielding composed of double-layered copper sheets – 4 μm thick each layer (or approximately half of skin depth for copper at 7T), with a 0.254 mm-thick dielectric in between (Polyflon, Germany) – was placed to cover the transmitting elements as described in Fig. 1. Split cuts were made in the copper sheets to effectively open the low-frequency eddy currents (induced as a result of the gradient fields) pathways, thus avoiding the potential fast gradient switching artifacts while

maintaining the RF characteristics associated with the Tx coil as described in [34]. The shields were extended to enclose the entire lower leg, except for a cavity on the top to accommodate the toes, thus allowing all sizes of feet and placement positions (Fig. 1d and e). The overall size of the coil is $250 \times 250 \times 290$ mm^3 (Fig. 1e).

2.3. Workbench measurements

The lengths of the inner rods for tuning/matching of the RF coil were estimated using finite-difference time-domain (FDTD) simulations, and then fined-tuned on the bench while the coil was loaded with a homogenous phantom – that corresponds to the averaged values of permittivity and conductivity of the Duke virtual family model at 297 MHz. The coupling of the RF coil is inherently high by its design [28]; therefore, changing one rod can affect all the channels. The s-matrix was measured using a network analyzer (Model E5062A, manufactured by Agilent Technologies).

2.4. FDTD simulations

The coil structure was modeled using Matlab (Mathworks, USA), and the FDTD grid was exported in a regular-spaced grid with $300 \times 300 \times 304$ Yee-cells and resolution of ~1.6 mm in all directions: X, Y, and Z. A validated in-house developed finite-difference time-domain (FDTD) software [35] was used to simulate the RF behavior of the coil/shields on a homogeneous phantom (Fig. 1c) and the anatomically detailed human lower leg model (Fig. 1d). The FDTD package incorporates true transmission line modeling for capturing the mechanism of excitation and reception, and, therefore, accurately predicting coil input impedance and coupling between coil elements [27,28,36,37].

The pulse used in the FDTD model was a modified differentiated Gaussian pulse with a period of 5.7 ns. The temporal resolution was ~3 ps and the simulation ran for 100.000 times steps, what is equivalent to 50 periods of the pulse, which was enough time to achieve steady state. The transmission line voltage (V) and current (I) in the time domain were stored and the s-parameters were calculated based on the transmit and reflected signal in the channels and the isolated input pulse.

The human lower leg model was extracted from the Duke model, and the homogenous phantom was simulated with relative permittivity of 39 and conductivity of 0.49 S/m, both values derived from the average values of the lower leg Duke model. The FDTD software generates the frequency domain (by Discrete Fourier Transform (DFT) of

the time domain data) of the Electric (E) and Magnetic (B) fields (in all directions of the Cartesian space). Each individual channel was simulated using a local cluster computer, 6 threads per channel, totaling about 8 h of computational time. The B_1^+ field was extracted and the associated SAR was calculated by Eq. (1) and averaged per 10 g of tissue.

$$SAR(x,y,z) = \frac{0.5^* \sigma(x,y,z)^* |\overline{E}|^2 (x,y,z)}{\rho(x,y,z)} \tag{1}$$

where σ is the conductivity in S/m, $\overline{E}$ is the electric field vector in V/m, ρ is the density in kg/m^3, and x,y,z are the positions in the Cartesian coordinates.

In addition to SAR values, the B_1^+ field distribution was evaluated using three metrics: 1) coefficient of variation (CV), which is a global homogeneity metric defined by the standard deviation divided by the mean of the signal in a region of interest; 2) maximum of the signal divided by the minimum (max/min), which accounts for local signal voids and bright spots; and 3) mean value of the signal, which measures the efficiency of the RF coil.

2.5. MRI experiments

The coil was tested in a 7T Human Scanner (Siemens Magnetom, Germany). A transmit/receive (T/R) switch box was utilized so that the same RF coil could be used to transmit and receive signal. The system can operate either in the single-channel mode, using a 4-way Wilkinson power splitter, or it can use the pTx mode available in the scanner to operate as a 4-channel transmit array. In the combined mode, constant phase shifters (with 90-degree increments) were added in the transmission lines to produce 4-port quadrature excitation.

B_1^+ mapping was acquired in a homogeneous cylindrical phantom (Fig. 1f) and in-vivo. The phantom is composed of 80% of denatured ethanol, 20% of water, and 9.85 g/L of sodium chloride [38]. The in-vivo scans were conducted under a study approved by the University of Pittsburgh Institutional Review Board. The sequence used was a saturated turbo FLASH with the following parameters: TE/TR = 1.09/ 3000 ms, resolution 3.1 × 3.1 × 3.1 mm^3, FOV 112 × 200, 36 × 64 acquisition matrix, six flip-angles for pre-saturation variating from 0 to 90°, total time of scan of 6 min. The data was then fitted to a cosine function using MATLAB and the B_1^+ map was calculated and scaled for a total power input of 1 W (i.e., 0.25 W in each excitation port).

Preliminary in-vivo image acquisition (without the use of a dedicated Rx-only insert) was performed using the 3D T2-DESS sequence, with the following parameters: TE/TR = 5/20 ms, resolution 0.62 × 0.62 × 0.62 mm^3, FOV 200 × 200, 320 × 320 acquisition matrix, 25° of flip-angle, acquisition time = 13:56 min, and reference voltage = 300 V.

3. Results

3.1. Scattering parameters: simulations and bench measurements

Using the homogeneous cylindrical phantom as a load, a reflection coefficient (S_{xx}) lower than − 20dB was achieved (experimentally and with FDTD simulations) for all 4 channels. The comparison between the simulated and measured scattering parameters from one representative channel is shown in the Fig. 2a and b. Figure c shows the measured s-matrix for all four channels of the designed RF coil. The mean measured reflection coefficient was − 30.4dB, while the average coupling among opposite ports (e.g. S13 and S24) was − 4.11dB and the average coupling among adjacent ports (e.g. S12, S23, …) was − 9.56dB. Note that high coupling between opposite ports is a unique characteristic of the TTT coil family, which happens at the cost of reduced B_1^+ per input power, but promotes B_1^+ homogeneity and RF field consistency with different loads, as demonstrated in prior studies [27–29,33,39].

3.2. Simulated and measured B_1^+ distributions in the homogenous phantom

Fig. 3a presents the B_1^+ field distribution, normalized for 1 W of total input power. The average simulated B_1^+ field intensities on the dotted lines are 0.75 μT, 0.74 μT and 0.76 μT in the sagittal, coronal and axial planes respectively. The measured B_1^+ field intensities are shown in the Fig. 3b and have the average values, on the dotted lines, of 0.57 μT, 0.58 μT and 0.61 μT for the sagittal, coronal and axial planes, respectively. The simulated and measured B_1^+ fields from the individual channels are shown in the Fig. 3d and e, respectively.

3.3. Simulated B_1^+ and SAR in the anatomically detailed lower leg human model, in-vivo B_1^+ mapping and image acquisition

The simulated B_1^+ field and SAR distributions with the lower human leg model are shown in the Fig. 4a and e respectively, both scaled for 1 W of total input power. The peak SAR was 0.34 W/kg for 10 g while the average SAR was 0.07 W/kg for 10 g over the whole lower leg. The in-vivo B_1^+ mapping is shown in the Fig. 4c. The conductivity and relative permittivity maps are shown in the Fig. 4b and d respectively. Fig. 4f shows the three regions of interest (ROI) used to calculate the stats of the simulated B_1^+ fields in the foot/ankle. For the mid foot, the stats are: CV = 28.8%, max/min = 8.13 and mean = 0.43 μT. For the calcaneus, the stats are: CV = 15.6%, max/ min = 2.76 and mean = 0.56μT. In the ankle, the stats are: CV = 23.9%, max/min = 5.34 and mean = 0.33 μT. For the in-vivo measurements (Fig. 4c), the mean B_1^+ is equal to 0.29 μT, while the average over the entire foot from simulations is equal to 0.42 μT. Fig. 4g shows a preliminary in-vivo image acquisition in a healthy subject.

4. Discussion

The lack of Tx body coil for 7T MRI forces the development of transmit coils dedicated for certain parts of the body. Due to the absence of commercial RF coil specific for foot/ankle at 7T, most sites use knee coils [7,18–22] or head coils [23–26] for imaging the foot/ankle. This situation is not optimal for several reasons. In the case of knee coils (usually have a cylindrical shape and were developed to close fit a knee), the foot has to stay in a high angle position (the recommended position is < 20 degrees of flexion [5]). This makes imaging unviable in cases like fracture or severe disease that impairs the movement of the foot. In the case of head coils, different sizes of foot may not fit due to the limited space available. The proposed TTT Tx coil has its elements positioned in the XY plane of the scanner; therefore, the foot and ankle can be imaged in a relaxing position. Furthermore, the proposed TTT RF coil does not have any lumped elements as it utilizes distributed capacitances, which help in terms of robustness and manufacturing. Due to the relatively large size and the gap in the RF shielding (Fig. 1d), any size of foot and lower leg can be scanned. Moreover, it is possible to adjust the position of the foot based on the region of interest.

An accurate simulation of the coil and the transmission lines is essential to ensure its performance and to predict SAR, since the in-vivo local SAR cannot be accurately measured in real time by the MRI scanner. The precise modeling of the true transmission line excitation was demonstrated by the close matching of the simulated and measured scattering parameters in Fig. 2a and b, respectively. Slight differences in the offset of transmission for opposite ports (S13) can be explained by losses in the system that were not included in the simulations, such as losses in the cables, coil copper, and connectors. The high coupling between opposite ports in the array (S13) may decrease the coil efficiency, yet other studies have demonstrated its potential to increase the B_1^+ fields homogeneity, decrease SAR per mean B_1^+ intensity and increase load insensitivity [27,28,33].

The comparison between the measured and simulated B_1^+ in the homogeneous phantom is highly favorable. Although the model approximates the phantom to a cylindrical structure (the real phantom
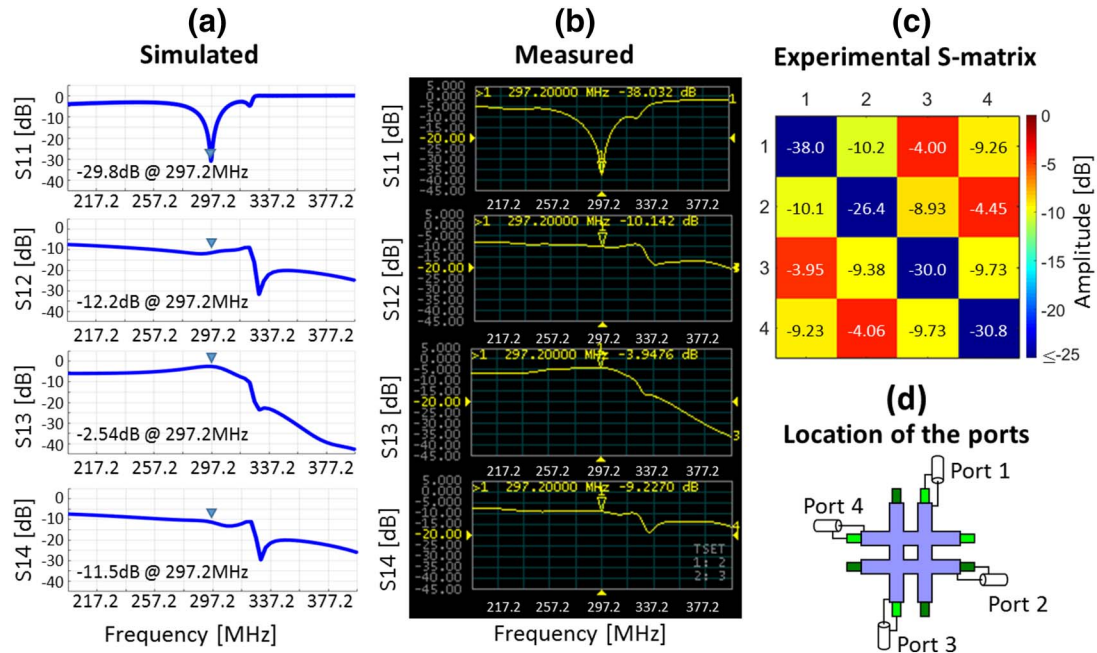
Fig. 2. Scattering parameters of the designed RF coil. In (a) the results from FDTD simulations of channel 1. In (b) the experimental measurements of transmit and reflection coefficients of channel 1. In (c) the experimental s-matrix with the measurements from the 4 channels. In (d), the locations of the ports used in the s-parameters simulation and measurement.
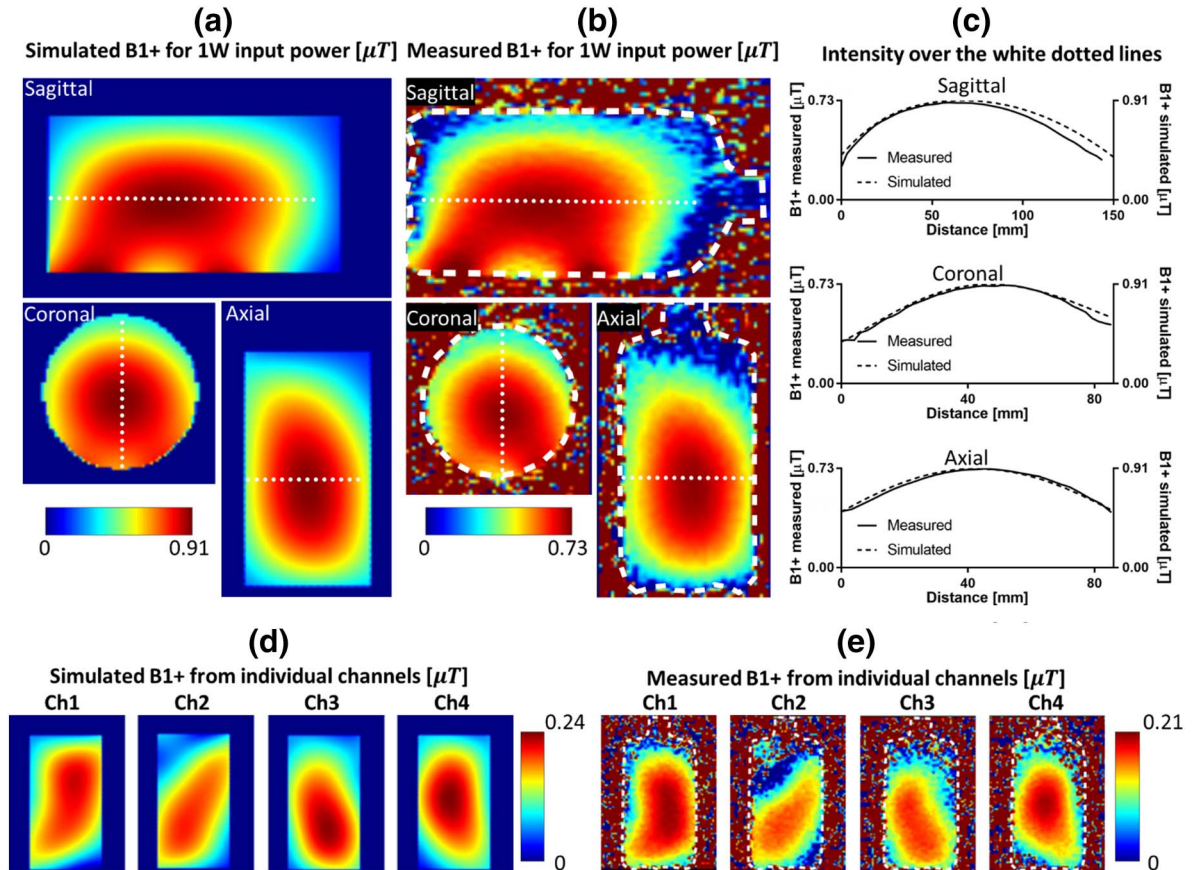

Fig. 3. Simulations and measurements in a homogenous phantom with relative permittivity 39 and conductivity 0.49 S/m. In (a), the simulated B_1^+ map for 1 W of total input power, calculated from FDTD simulations; In (b), the measured B_1^+ for 1 W of total input power; In (c), the intensity plots of the B_1^+ maps over the dotted lines on the figures, in all planes; In (d), the axial slices of the simulated individual channels scaled for 0.25 W of input power; In (e), the measured B_1^+ maps of the individual channels scaled for 0.25 W of input power.

has a bottleneck to facilitate the filling), the pattern was almost identical (Fig. 3a and b). Graphs with the B_1^+ intensity over the dotted line were plotted in all 3 planes, and further reinforced the similarities

between measured and simulated data. The difference in the scale (about 20%) can be explained by the losses in the cables, coil plug, T/R switch, 4-way splitter and connectors in the coil, that are not included
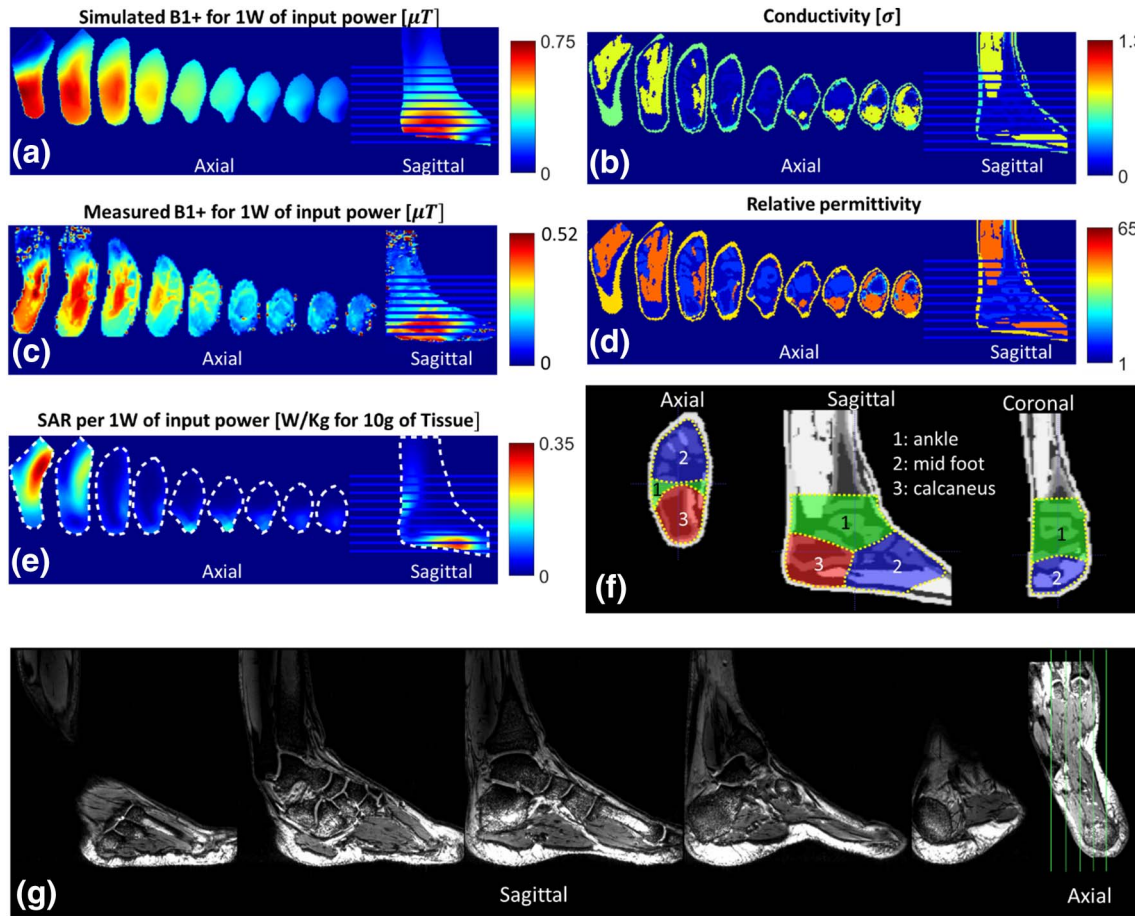
Fig. 4. Simulations of the Tx coil with the foot model extracted from Duke virtual family. In (a), the simulated B_1^+ field distribution for 1 W of total input power (not accounting for losses in the cables/splitter/TR box); In (b), the conductivity map for the tissues at 297 MHz; In (c), the in-vivo B_1^+ mapping, scaled for 1 W of total input power; In (d), the relative permittivity map for the tissues at 297 MHz; In (e), the SAR map per 1 W of total input power; In (f), the regions of interest used to calculate the statistics of the B_1^+ distribution, plotted over the permittivity maps in the three planes; In (g), multiple slices of an in-vivo 3D T2-DESS acquisition at 7T, with a resolution of 0.6 mm isotropic.

in the simulations. The same level of similarities is seen in the B_1^+ mapping of the individual channels.

The comparison between in-vivo measured and simulated B_1^+ fields reveals a similar pattern of the field distribution. The in-vivo measured B_1^+ mean is about 30% lower, while in the homogenous phantom this difference was about 20% (attributed to splitters/cables/TR box). The additional difference in the mean value can be explained by differences in the position of the foot inside the coil and by the high amount of bones in the foot, which makes the B_1^+ measurement challenging due to the low signal produced by the bone tissues.

Based on the simulated mean values of the B_1^+ in different regions of the lower leg, it will be necessary to apply 273 V, 210 V and 356 V, respectively, on the mid foot, calcaneus and ankle to produce an average of 180° flip angle, using 1 ms square-shaped pulse (equivalent to 11.74μT) in these regions of interest.

There are limited publications about development of RF coils for 7T MRI specific for ankle and foot in the literature. Orzada et al. [17] developed an open design transceiver using 8 microstrip elements. Although 20% of deviation in the B_1^+ in a human foot was reported, very limited number of pixels were acquired rendering the experimental measurements to be less accurate. The highest peak SAR was reported to be 4.73 W/kg for 10 g per 1 W input power as opposed to 0.34 W/kg for 10 g per 1 W input power with the TTT coil (a ratio of 13.91). The peak B_1^+ in the TTT simulations however was 11.25 μT for 150 V input (1 ms pulse duration) against 32 μT experimentally measured by Orzada et al. [17]. While this shows increase of power by a factor of 8.09 with the TTT design (in order to achieve the same average B_1^+), the

peak SAR (which would approach the FDA/IEC limits before the average SAR [40]) is 13.91 times lower, and therefore the SAR efficiency is substantially better with the TTT coil. While Wright et al. [16] developed an innovative Helmholtz pair transmit-only with a 4-channel Rx-only array, no metric (e.g., B_1^+ mean or peak, and/or SAR in the foot model simulations) that can be used to compare directly with this work was reported. Furthermore, the homogenous cylindrical phantoms (relative permittivity of ~78 and a conductivity of ~0.66 S/m) used in [16] are not comparable to the phantom utilized in this work (in the simulations and experiments) as it has a relative permittivity of 39 and a conductivity of 0.49 S/m, representing the average values of the lower leg of the Duke model.

The coil was able to produce high resolution preliminary images using the 3D T2-DESS sequence. Further improvements in this work can be done by building an Rx-only insert with a proper decoupling system that can be integrated with the proposed Tx coil (not suitable for optimal receive operation due to its inherent high coupling). The Rx-only insert should not significantly affect the RF performance of the Tx coil [36], and shall improve SNR for performing human imaging experiments. Moreover, RF shimming can potentially be used to improve the B_1^+ homogeneity and reduce SAR. Finally, the position of the foot can be fine-tuned to assure the best coil performance.

5. Conclusion

In this study, we designed and evaluated a new 4-channel TTT Tx RF coil for foot and ankle imaging at 7T MRI. Excellent agreement is

observed between the RF simulations and experimental measurements in a homogeneous phantom. Homogenous B_1^+ field distribution as well as acceptable peak/global SAR levels were observed in FDTD simulations of an anatomically detailed lower leg human model. In-vivo experiments were performed successfully. Future work will include the construction of an Rx-only array for high SNR and parallel imaging.

Acknowledgements

References

[1] Bangerter NK, et al. Quantitative sodium magnetic resonance imaging of cartilage, muscle, and tendon. Quant Imaging Med Surg 2016;6(6):699–714.

[2] Krug R, et al. Imaging of the musculoskeletal system in vivo using ultra-high field magnetic resonance at 7 T. Invest Radiol 2009;44(9):613–8.

[3] Kogan F, Fan AP, Gold GE. Potential of PET-MRI for imaging of non-oncologic musculoskeletal disease. Quant Imaging Med Surg 2016;6(6):756–71.

[4] Alizai H, Chang G, Regatte RR. MRI of the musculoskeletal system: advanced applications using high and ultrahigh field MRI. Semin Musculoskelet Radiol 2015;19(4):363–74.

[5] Bright A. Planning and positioning in MRI. Australia: Elsevier; 2011.

[6] Oei L, et al. Quantitative imaging methods in osteoporosis. Quant Imaging Med Surg 2016;6(6):680–98.

[7] Juras V, et al. Histological correlation of 7 T multi-parametric MRI performed in ex-vivo Achilles tendon. Eur J Radiol 2013;82(5):740–4.

[8] Bangerter NK, et al. Quantitative techniques for musculoskeletal MRI at 7 Tesla. Quant Imaging Med Surg 2016;6(6):715–30.

[9] Kraff O, Quick HH. 7T: physics, safety, and potential clinical applications. J Magn Reson Imaging 2017.

[10] Welsch GH, et al. Magnetic resonance imaging of the knee at 3 and 7 tesla: a comparison using dedicated multi-channel coils and optimised 2D and 3D protocols. Eur Radiol 2012;22(9):1852–9.

[11] Moser E, et al. 7-T MR—from research to clinical applications? NMR Biomed 2012;25(5):695–716.

[12] Robitaille P-M, Berliner L. Ultra high field magnetic resonance imaging. 26. Springer Science & Business Media; 2007.

[13] Schmitter S, et al. Cerebral TOF angiography at 7T: impact of B1 (+) shimming with a 16-channel transceiver array. Magn Reson Med 2014;71(3):966–77.

[14] Metzger GJ, et al. Dynamically applied B1 + shimming solutions for non-contrast enhanced renal angiography at 7.0 Tesla. Magn Reson Med 2013;69(1):114–26.

[15] Deniz CM, et al. Maximum efficiency radiofrequency shimming: theory and initial application for hip imaging at 7 tesla. Magn Reson Med 2013;69(5):1379–88.

[16] Wright AC, et al. Helmholtz-pair transmit coil with integrated receive array for high-resolution MRI of trabecular bone in the distal tibia at 7T. J Magn Reson 2011;210(1):113–22.

[17] Orzada S, et al. Open design eight-channel transmit/receive coil for high-resolution and real-time ankle imaging at 7 T. Med Phys 2011;38(3):1162–7.

[18] Trattnig S, et al. Advanced MR methods at ultra-high field (7 Tesla) for clinical musculoskeletal applications. Eur Radiol 2012;22(11):2338–46.

[19] Juras V, et al. Regional variations of T(2)* in healthy and pathologic Achilles tendon in vivo at 7 Tesla: preliminary results. Magn Reson Med 2012;68(5):1607–13.

[20] Juras V, et al. Comparison of 3T and 7T MRI clinical sequences for ankle imaging. Eur J Radiol 2012;81(8):1846–50.

[21] Domayer SE, et al. Cartilage repair of the ankle: first results of T2 mapping at 7.0 T after microfracture and matrix associated autologous cartilage transplantation. Osteoarthritis Cartilage 2012;20(8):829–36.

[22] Deligianni X, et al. High-resolution Fourier-encoded sub-millisecond echo time musculoskeletal imaging at 3 Tesla and 7 Tesla. Magn Reson Med 2013;70(5):1434–9.

[23] Han M, et al. Depiction of Achilles tendon microstructure in vivo using high-resolution 3-dimensional ultrashort echo-time magnetic resonance imaging at 7 T. Invest Radiol 2014;49(5):339–45.

[24] Theysohn JM, et al. MRI of the ankle joint in healthy non-athletes and in marathon runners: image quality issues at 7.0 T compared to 1.5 T. Skeletal Radiol 2013;42(2):261–7.

[25] Krug R, et al. In vivo ultra-high-field magnetic resonance imaging of trabecular bone microarchitecture at 7 T. J Magn Reson Imaging 2008;27(4):854–9.

[26] Banerjee S, et al. Rapid in vivo musculoskeletal MR with parallel imaging at 7T. Magn Reson Med 2008;59(3):655–60.

[27] Kim J, et al. Development of a 7 T RF coil system for breast imaging NMR Biomed 2016.

[28] Kim J, et al. Experimental and numerical analysis of B1 + field and SAR with a new transmit array design for 7T breast MRI. J Magn Reson 2016;269:55–64.

[29] Ibrahim TS, et al. 20-To-8 channel Tx array with 32-channel adjustable receive-only insert for 7T head imaging. International Society of Magnetic Resonance in Medicine; 2013. [Salt Lake City, Utah].

[30] Ibrahim TS, et al. Tic Tac Toe: highly-coupled, load insensitive Tx/Rx array and a quadrature coil without lumped capacitors. Intl. Soc. Mag. Reson. Med. 2008.

[31] Zhao Y, et al. Simultaneous excitation of distinct electromagnetic modes using a Tx array. ISMRM. 2013. [Salt Lake City, US].

[32] Raval S, et al. In-vivo (8x4) 32-ch Tx-only body array for UHF MR. In Proc. of the 25th International Society of Magnetic Resonance in Medicine Annual Meeting. 2017. [Honolulu, Hawaii, USA].

[33] Zhao Y, et al. 3D eigenmodes optimizations for 3D imaging at 7T. The 23nd International Society of Magnetic Resonance in Medicine Annual Meeting. 2015. [Toronto, Canada].

[34] Zhao Y, et al. Dual optimization method of radiofrequency and quasistatic field simulations for reduction of eddy currents generated on 7T radiofrequency coil shielding. Magn Reson Med 2014.

[35] Tang L, Hue YK, Ibrahim TS. Studies of RF shimming techniques with minimization of RF power deposition and their associated temperature changes. Concepts Magn Reson Part B Magn Reson Eng 2011;39B(1):11–25.

[36] Krishnamurthy N, Zhao T, Ibrahim TS. Effects of receive-only inserts on specific absorption rate, B1 (+) field, and Tx coil performance. J Magn Reson Imaging 2014;39(2):475–84.

[37] Ibrahim TS, Hue YK, Tang L. Understanding and manipulating the RF fields at high field MRI. NMR Biomed 2009;22(9):927–36.

[38] Wood S, et al. Design and fabrication of a realistic anthropomorphic heterogeneous head phantom for MR purposes. PLoS One 2017;12(8).

[39] Raval SB, et al. Ultra-high-field RF coil development for evaluating upper extremity imaging applications. NMR Biomed 2016;29(12):1768–79.

[40] Fiedler TM, Ladd ME, Bitz AK. SAR simulations & safety. Neuroimage 2017.